The Astrophysical Journal Letters, 889:L12 (7pp), 2020 January 20 https://doi.org/10.3847/2041-8213/ab6169

Deep *Hubble Space Telescope* Imaging on the Extended Lyα Emission of a QSO at $z = 2.19$ with a Damped Lyman Alpha System as a Natural Coronagraph

Jiani Ding[1], Zheng Cai[2], J. Xavier Prochaska[2,3], H. Finley[4,5], Xiaohui Fan[6], Zheng Zheng[7], H. Fathivavsari[8], and P. Petitjean[8]

[1] Department of Astronomy and Astrophysics, UCO/Lick Observatory, University of California, 1156 High Street, Santa Cruz, CA 95064, USA
[2] Department of Astronomy and Center for Astrophysics, Tsinghua University, Beijing 100084, China; zcai@mail.tsinghua.edu.cn
[3] Kavli Institute for the Physics and Mathematics of the Universe (Kavli IPMU; WPI), The University of Tokyo, 5-1-5 Kashiwanoha, Kashiwa, Chiba Prefecture 277-8583, Japan
[4] Université de Toulouse, UPS-OMP, 31400 Toulouse, France
[5] IRAP, Institut de Recherche en Astrophysique et Planétologie, CNRS, 14 avenue Édouard Belin, 31400 Toulouse, France
[6] Steward Observatory, University of Arizona, Tucson, AZ 85721, USA
[7] Department of Physics & Astronomy, University of Utah, Salt Lake City, UT 84112-0830, USA
[8] Institut d'Astrophysique de Paris, Universite Paris 6-CNRS, UMR7095, 98bis Boulevard Arago, F-75014 Paris, France
Received 2019 September 11; revised 2019 November 13; accepted 2019 December 4; published 2020 January 20

Abstract

Recent observations suggest that proximate damped Lyα (PDLA) systems can be used to study the host galaxies of quasi-stellar objects (QSOs), because the PDLAs can block the bright point-spread function from central QSOs. Using six orbits of narrowband imaging with *Hubble Space Telescope* (*HST*)/WFC3, we present the first high-resolution narrowband image of the Lyα emission in the PDLA trough of the QSO SDSS J115432.67–021537.9. We detect one major component and one minor component in the narrowband imaging. Combining the *HST*/WFC3 imaging with deep *Magellan*/MagE spectra, we measure that the Lyα flux $F_{\rm Ly\alpha} = 1.56 \pm 0.10 \times 10^{-16}$ erg s^{-1} cm^{-2}, which is among the luminous ($\approx$2.7 $L^{\star}_{\rm Ly\alpha}$) Lyα emitters at z= 2.19. The Lyα-based star formation rate is $\sim$7 $M_{\odot}$ yr^{-1}. These observational results favor that the star formation from the host galaxy could be the main mechanism powering the Lyα emission. This new method sheds light on the study of the kinematic structure and the spatial distribution of the extended Lyα emitting regions around the QSO host.

Unified Astronomy Thesaurus concepts: Quasars (1319); Quasar absorption line spectroscopy (1317); HST photometry (1317)

1. Introduction

High redshift quasi-stellar object (QSO) host galaxies are crucial for studying the coevolution of massive galaxies and their central black holes (Schramm et al. 2008; McLeod & Bechtold 2009; Targett et al. 2012; Matsuoka et al. 2015). The relation between black hole mass and bulge stellar mass connects the star formation history of the host galaxies with the evolution of the central black holes (e.g., Gebhardt et al. 2000; McConnell & Ma 2013; Bennert et al. 2015; Reines & Volonteri 2015). Studying the host galaxies casts light on segregating the star formation process and the black hole growth, leading to a better understanding of galaxy evolution and providing strong tests of merger-driven evolutionary models (e.g., Hopkins et al. 2006). To better explore host galaxies around QSOs, a technique has been proposed to utilize proximity damped Lyα absorbers (PDLAs) at approximately the same redshift as the QSOs. The DLA clouds are expected to cover the broad-line region of the QSO ($\sim$parsec scales) but leave the extended emission unshielded at greater than about 1 kpc scales. Therefore, DLAs can be used as natural coronagraphs, to reveal the extended emission from QSO hosts (e.g., Hennawi et al. 2009; Finley et al. 2013; Cai et al. 2014; Fathivavsari et al. 2015, 2016, 2018). By analyzing $\geqslant$2,000 high signal-to-noise ratio (S/N) DLAs in Sloan Digital Sky Survey (SDSS)-III, Cai et al. (2014) indicated that due to the correlation between the residual intensities in the DLA troughs and the quasar luminosities, the residual fluxes detected in the DLA trough are more likely from QSO hosts rather than DLA galaxies.

Finley et al. (2013) identified 26 $z > 2$ PDLAs that have narrow Lyα emission detected in the PDLA trough with a FWHM $\sim$ 500 km s^{-1}. There are several possible origins for this extended emission, namely: Lyα emission from the star-forming regions in the QSO host galaxy, fluorescent recombination radiation powered by the QSO, or Lyα emission from the DLA host. Fathivavsari et al. (2016) conducted a detailed spectroscopic study of a sample of six QSOs with PDLA and suggested that three of the targets have Lyα luminosities similar to those of bright LAEs ($L = 2 - 4\,L^{*}_{\rm Ly\alpha}$), consistent with the expected Lyα emission from a QSO host galaxy.

To further investigate this technique, we conduct a high-resolution, direct-imaging program. In this paper, we present a pilot imaging on J1154–0215, one PDLA at $z = 2.1853$ reported by Finley et al. (2013) that has Lyα emission perfectly residing within the *Hubble Space Telescope* (*HST*) WFC3/UVIS FQ387N narrowband filter. Using six orbits of high-resolution *HST* imaging and deep spectroscopic measurements from the *Magellan*/MagE spectrum from Fathivavsari et al. (2016), we discuss possible origins of the extended Lyα emission from J1154–0215. This Letter is organized as follows. In Section 2, we discuss our *HST* observations and data reduction. In Section 3, we measure the column density of the DLA and the Lyα flux of the target and discuss its morphology. In Section 4, we discuss the basic physical properties of the DLA and possible physical scenarios for the origin of the Lyα emission. Throughout the paper, we adopt a flat lambda-cold dark matter cosmology with $\Omega_{\lambda} = 0.7$, $\Omega_{m} = 0.3$ and $H_0 = 70$ km s^{-1} Mpc^{-1}.

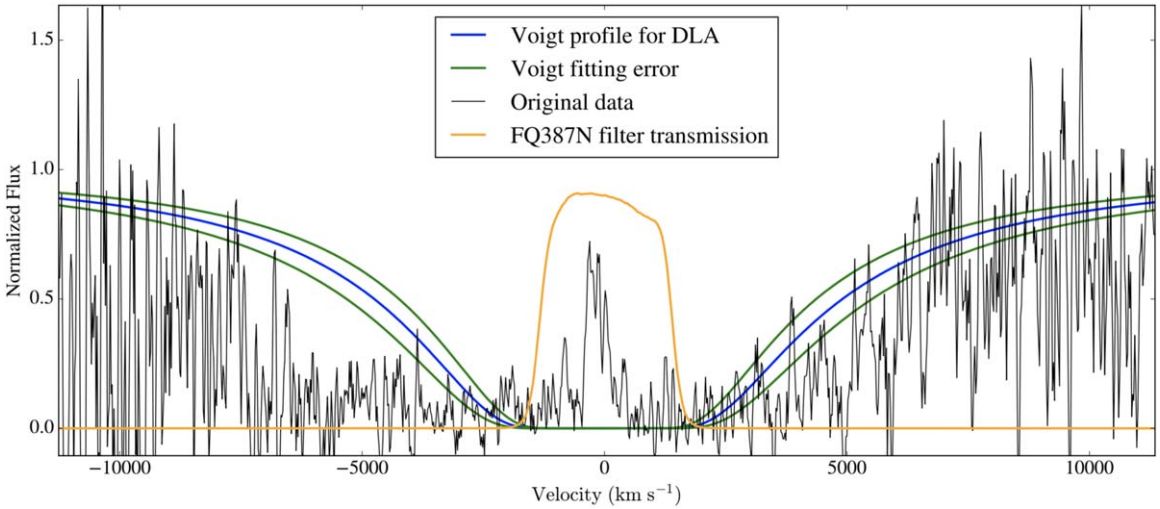

Figure 1. Voigt fitting (light blue) with error (green) for the target J1154–0215. The filter response (orange curve) for the WFC3 FQ387N filter and the original data (black curve) are also overplotted in the graph. The absorption redshift for this target is $z = 2.1853$.

2. Observation and Data Reduction

2.1. Magellan/*MagE Spectroscopy*

Figure 1 shows the spectroscopic data of J1154–0215 from Fathivavsari et al. (2016). The median S/N around the Lyα emission is $\sim$3 pixel^{-1} and the resolution is ($R \sim 4000$). The reduction and data analysis process for the final spectrum are detailed in Fathivavsari et al. (2016). The MagE spectroscopy allows us to measure the metal lines associated with this PDLA. The metal-line diagnostic will constrain the distance between the absorbers and the QSO (see details in Section 4.1).

2.2. HST *Narrowband Imaging*

We use six orbits (about 17,000 s) on the FQ387N narrowband observation of the QSO J1145–0215, which allows us to detect the Lyα flux at the 15σ level in the FQ387N filter.

We distribute our observations into two individual visits, each with three orbits. A standard three-point dither sequence is applied to populate each orbit. We conduct the deep *HST*/WFC3 narrowband FQ387N imaging of J1154–0215 as explained above. The redshift for the Lyα emission $z_{\rm em} = 2.181$ and the redshift for the absorber, $z_{\rm abs} = 2.1853$, which are measured in Fathivavsari et al. (2016). In Figure 1, we plot the spectrum with the filter response curve of the FQ387N filter ($\lambda_c = 3874$ Å, FWHM = 34 Å) and the Voigt profile fitting for the DLA. The filter lies within the DLA trough and the Lyα emission is included in the filter.

The data reduction is conducted using WFC3/UVIS (Koekemoer et al. 2002), and the detailed procedures follow Cai et al. (2011, 2015). To optimize the output data quality, we choose a final output pixel scale of 0.″03 instead of an initial pixel scale 0.″04 and final pixfrac parameter 0.7 (shrinking pixel area) after different trials of combinations of parameters. The final output images we obtained from *HST* for J1145–0215 are shown in the upper left panel of Figure 2.

3. Results

3.1. *The Detection of Extended Ly*α *Emission by* HST

In our *HST* narrowband image, we detect spatially resolved, diffuse Lyα emission. Using SExtractor (Bertin & Arnouts 1996), we measure the Lyα flux using an elliptical aperture with a Kron factor of 2.5 (0.″075) (magenta elliptical in upper left panel in Figure 2). The flux density of the source is $F_{\rm FQ387N} = 6.2 \pm 0.2 \times 10^{-18}$ erg s^{-1} cm^{-2} Å^{-1} (total flux $F_{\rm total} = 2.11 \pm 0.07 \times 10^{-16}$ erg s^{-1} cm^{-2}), corresponding to an AB magnitude of 22.68 ± 0.04.

In the upper left panel of Figure 2 we overplot the QSO position (dark point) with its error (green dashed circle). Note that our *HST* narrowband completely resides in the DLA dark trough. Thus, we do not have QSO continuum flux from our *HST* observations. The SDSS provides the QSO continuum position. We use two stars in the *HST* field to correct the offset between the SDSS and the *HST* coordinate systems (assuming the rotational offset is zero). We find that the offset between *HST* and SDSS is $0.''09 \pm 0.''1$. We also examine the morphology of this source. The *HST* image and the circularly averaged surface brightness (SB) profile shown in the lower left panel of Figure 2 suggest that we detect two resolved components, and we use two Sérsic components (right in Figure 2) to fit J1154–0215. We measure an effective radius of 0.29 ± 0.05 kpc for the major component and a radius of 1.52 ± 0.6 kpc for the minor component. The contour of the SB of the source from the Sérsic components model fitting is shown in the upper right panel of Figure 2. The residual of the fitting for this model is shown in the lower right panel of Figure 2. We also use two Gaussian components to repeat the above fitting and recover similar results of one major component and one minor component. The detailed parameters of the two models are shown in Table 1.

3.2. *DLA Column Density and Ly*α *Emission Flux from MagE Spectrum*

For the MagE spectra from Fathivavsari et al. (2016), we plot the spectra with the filter response curve of the FQ387N filter and the Voigt profile fitting with the error for the DLA in

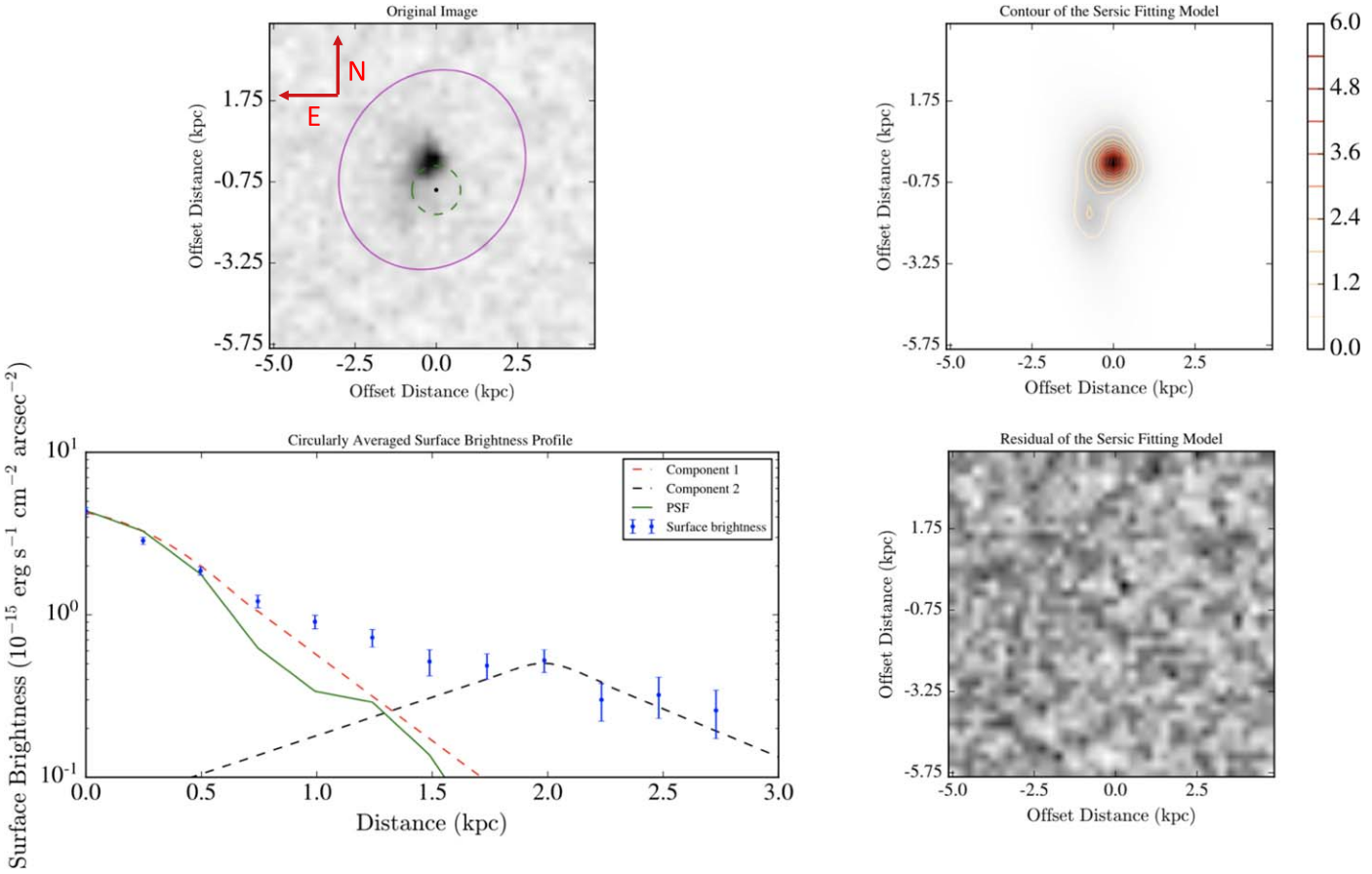

Figure 2. Final combined image and model of the source. Top left panel: the final combined image of the source. The aperture we used for photometric measurements is labeled in magenta. The position of the QSO is labeled as a black dot and the error of the position is in green. Bottom left panel: the circularly averaged surface brightness (SB) profile (data points labeled in blue) centered at the flux peak of the source. The PSF profile is labeled as green curve and renormalized to set the first data point of PSF profile and the profile for the source to have equal flux. The red and black dashed curves show the contributions from the two components for the source. Upper right panel: the Galfit model of the source for fitting two Sérsic components with the contours and color bar of the SB of this model. The value of the color bar is in units of 10^{-15} erg s^{-1} cm^{-2} arcsec^{-2}. Lower right panel: the residual of the Galfit model for fitting with two Sérsic components. The offset distances labeled in the axes of the images are offset distances from the flux peak of the target.

Figure 1. The spectral resolution is 75 km s^{-1}. We attain the H I column density for the DLA as $\log(N_{\rm HI}) = 21.76 \pm 0.1$, consistent with the value fitted by Fathivavsari et al. (2016). We further fit a double-Gaussian profile to the Lyα spectrum inside the DLA dark trough. The integrated Lyα emission flux is $F_{\rm Ly\alpha} = 1.56 \pm 0.10 \times 10^{-16}$ erg s^{-1} cm^{-2} from this spectrum. Moreover, we also detect and fit metal lines Si II 1260, Si* II 1264 in this spectrum (shown in Figure 3, with a detailed analysis in Section 4.1).

4. Discussion

In the following subsections, we discuss the physical properties of the DLA gas and the origin of the extended Lyα emission.

4.1. Size of the Cloud and the Distance to Nearby QSOs

From the high-resolution *HST* FQ387N imaging, we do not detect Lyα emission in the central QSO region, and we now refer to this region as a Lyα "void." This may be explained by the fact that a kiloparsec-scale optically thick cloud is located in the region of the Lyα emission "void." We construct a power-law model without DLA absorption for the SB profile centered at the quasar position (labeled in red in Figure 4). We then add the absorption from the DLA to the model and find the best-fitted model to the data of the SB profile[9] (model labeled in green and data labeled in blue in Figure 4). The two models (with and without DLA implemented) converge at $r \sim 1.5$ kpc. We thus infer that the cloud size optically thick to the Lyα emission is $\sim$1.5 kpc. Our conclusion also agrees with the physical extent (<10 kpc) of $\log(N_{\rm HI}) \geqslant 20.3$ absorption constrained by lensed quasar pairs in Cooke et al. (2010). The physical picture of the QSO, DLA cloud, and the "void" of Lyα emission are illustrated in the left panel of Figure 5.

From the last section, we also detect absorption lines, Si II 1260 and Si* II 1264 from the MagE spectrum arising from the ground state n and the excited state n^* of Si$^+$. For a single, homogeneous cloud, the column density ratio between the lines from the excited state and the lines from the ground state is equal to the corresponding volume densities ratio of the ions/atoms (Bahcall 1967; Silva & Viegas 2002; Prochaska et al. 2006), namely, $\frac{n^*}{n} = \frac{N^*}{N}$. This ratio may be determined by the ratio of the column density between Si* II 1264 and Si II 1260. Since the Si II 1260 line is saturated, we will put a lower limit

[9] We assume the optical depth τ of the target evolves as a function of the distance r ($\tau = {a_1}^* r^{(-\alpha)}$) from the quasar position and the SB profile evolve as ${a_2}^* e^{-\tau}$ + c, where a_1, α, a_2 and c are constants.

Table 1
Parameters of the Two Galfit Models for the Source

Model Name	Comp1 mag	Comp2 mag	Comp1 Effective Radius (kpc)	Comp1 Sérsic Index	Comp2 Effective Radius (kpc)	Comp2 Sérsic Index
Sérsic model	23.02 ± 0.07	23.82 ± 0.28	0.29 ± 0.05	4.43 ± 1.95	1.52 ± 0.6	2.49 ± 1.28
Gaussian model	23.22 ± 0.02	23.80 ± 0.07	0.62 ± 0.06	0.28 ± 0.12	2.97 ± 0.33	0.23 ± 0.05

Note. (1) The magnitude is AB magnitude. (2) The notation "comp" means "component."

on its column density. Since the b value and column density will be degenerated when fitting the line Si II 1260, we test a range of Doppler parameter (b) value and use the maximum b value ($b = 30\,\mathrm{km\,s^{-1}}$) to obtain a lower limit of the column density of $\log(N/\mathrm{cm^{-2}}) = 15.3$ for Si II 1260. We then fit Si* II 1264 with a fixed b value $= 30\,\mathrm{km\,s^{-1}}$ and attain the column density of $\log(N/\mathrm{cm^{-2}}) = 13.62 \pm 0.13$.[10] The results of the Voigt profile fitting of these absorption lines are shown in Figure 3.

If we assume the excited level is populated by indirect pumping of far-UV photons, Prochaska et al. (2006) derived a relation between $\frac{n^*}{n}$ (see Figure 7 in Prochaska et al. (2006)) and the far-UV flux. We can derive that $d = \sqrt{\frac{L}{F_{uv}4\pi}}$, where L is the quasar luminosity in the far-UV range ($8\,\mathrm{eV} < h\nu < 13.6\,\mathrm{eV}$), and F_{uv} is the far-UV flux determined from $\frac{n^*}{n}$ based on the relation of population ratio and intensity from Prochaska et al. (2006). The quasar luminosity L is computed by integrating a local power law through the far-UV frequency range ($\int a\nu^{-\alpha_Q} d\nu$), where a is a constant. The local power law in this integral is estimated by the SDSS u band and SDSS g band photometric result. We finally get $L = 1.33 \times 10^{45}\,\mathrm{erg\,s^{-1}}$. We infer $I_{uv} = 32\,\mathrm{erg\,s^{-1}\,cm^{-2}}$ from the ratio of the column density estimated by the pair of Si^+ lines. Based on the equation $d = \sqrt{\frac{L}{F_{uv}4\pi}}$, we finally get an upper limit of $d \leqslant 0.6$ kpc, with a lower limit on the column density of Si II 1260, which is consistent with the fact that this target has the highest Al III/Si II ratio reported for a PDLA in Fathivavsari et al. (2016), indicating that it may be close to the active galactic nucleus. The physical picture of the QSO and DLA position is illustrated in the right panel of Figure 5

4.2. The Origin of the Emitting Gas

Combining the photometric and *Galfit* fitting results of the final combined image with the reduced 1D spectrum, there are three main possible origins for the emitting gas for the Lyα emission: (1) emission from star-forming regions in the QSO host galaxy; (2) emission from star-forming regions in the DLA galaxy; (3) fluorescent Lyα emission from the optically thick gas cloud.

4.2.1. QSO Host Galaxies

We compute the luminosity of the Lyα emission for target J1154–0215 to be $5.71 \pm 0.33 \times 10^{42}\,\mathrm{erg\,s^{-1}}$. Most of the LAEs discussed in Ouchi et al. (2008) and Ciardullo et al. (2012) have a Lyα emission $< 5 \times 10^{43}\,\mathrm{erg\,s^{-1}}$, suggesting that the Ly$\alpha$ emission from this target may have similar luminosity as bright LAEs ($\sim 2.7\,L^{\star}_{\mathrm{Ly}\alpha}$). If we assume the Ly$\alpha$ emission is from the star-forming region of the host galaxy, we can estimate that the Lyα-based star formation rate (SFR) is $\sim 7\,M_{\odot}\,\mathrm{yr^{-1}}$ (e.g., Kennicutt 1998; Dijkstra & Westra 2010). Taking into account the effect of dust extinction and absorption by foreground H I gas, the SFR we computed may be a lower limit.

Assuming the Lyα emission originated from star-forming regions in the QSO host galaxy, the total fluxes F_{total} we measured inside the filter will be the sum of the UV continuum and the Lyα emission. Thus, we can estimate the UV continuum by subtracting the Lyα emission fluxes fitted by the spectrum from F_{total}. The resultant UV continuum is $F_{\mathrm{UV}} = 0.86 \pm 0.3 \times 10^{-16}\,\mathrm{erg\,s^{-1}\,cm^{-2}}$, which is at the level of $14 \times 10^{28}\,\mathrm{erg\,s^{-1}\,Hz^{-1}}$. Assuming a flat UV-slope, the UV-based SFR is $\sim 19\,M_{\odot}\,\mathrm{yr^{-1}}$ (Kennicutt 1998), which is consistent with the SFR inferred by the Lyα emission.[11] The $\mathrm{SFR_{UV}}$ is consistent with the results of $\sim$200 LAEs at $z \sim 2$ (Ouchi et al. 2008; Guaita et al. 2010; Ciardullo et al. 2012). In addition, Fathivavsari et al. (2016) suggest that this target exhibits typical features of LBGs (redshifted emission and blueshifted absorption). Also, the Lyα emission luminosity for our target does not exceed the luminosity of the brightest LBGs in Shapley et al. (2003). Therefore, it is likely that the emission is coming from star formation based on these calculations.

The asymmetric morphology of the target fitted by *Galfit* shows a major component and a minor component (see Figure 2). From the fitting models, we can see that the flux from the major component is twice that of the fluxes from the minor component. From the fitting result, the effective radius of the major component is approximately five times smaller than the minor component, suggesting that it is much more compact than the minor component. The simulation result of the minor merger from Lotz et al. (2010) also suggests that the remnants of a minor merger will show compact nuclei, which is consistent with our morphology results. Our current data may suggest that this QSO is associated with a merger event.

4.2.2. DLA Galaxies

From Fathivavsari et al. (2016), the metallicity of the associated DLA for J1154–0215 is $[\mathrm{Si\,II/H}] = -1.70$. Based on the relation between metallicity and stellar mass inferred in Møller et al. (2013) and the relation between stellar mass and SFR demonstrated in Yates et al. (2012; assuming the DLA system as a DLA galaxy), this low metallicity may correspond to a much lower SFR ($<1\,M_{\odot}\,\mathrm{yr^{-1}}$) compared to the SFR estimated from Lyα emission and UV emission. The Lyα emission and the low metallicity DLA may be from separate

[10] Since the S/N of the spectrum is low in the region these absorption lines located, we fit a Voigt profile for a fixed b value by using curvefit in the scipy package. The 1σ error of the column density is estimated from the fitting error. These lines vary within the reported uncertainty when b changes from 20 to 30 km s^{-1}.

[11] $\mathrm{SFR_{UV}} = \frac{f_{1500} \times 4\pi d_L^2 \times 1.4 \times 10^{-28}}{1+z} M_{\odot}\,\mathrm{yr^{-1}}$ (Kennicutt 1998).

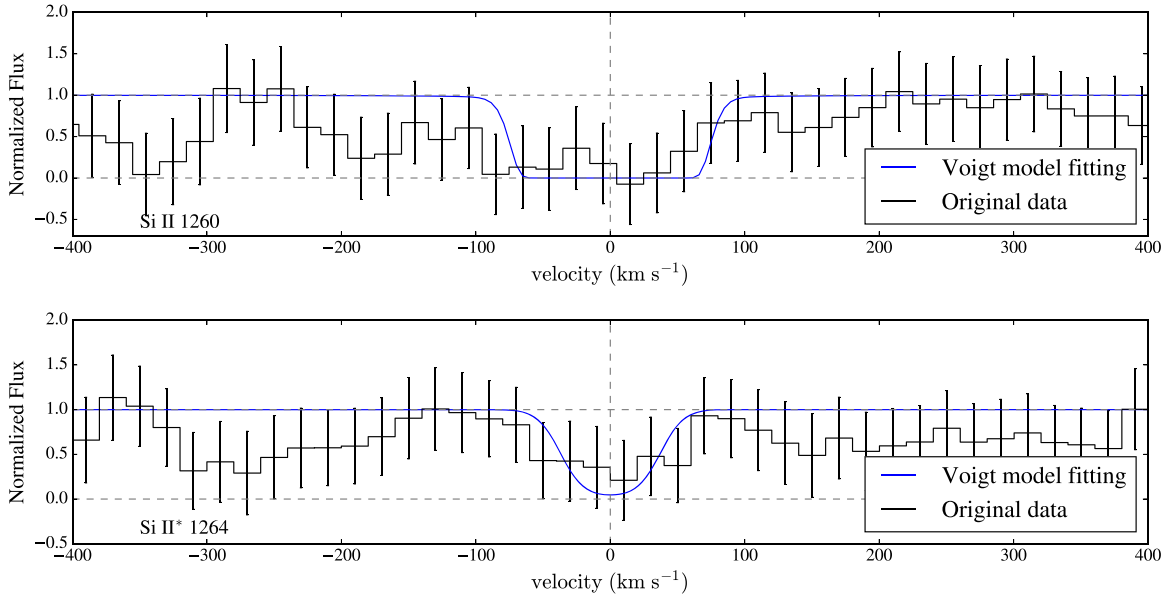

Figure 3. Velocity plots and best-fit Voigt profile of the species detected in the DLA redshift ($z = 2.18532$). The original data are labeled in black with an error bar, and the Voigt profile is labeled in blue.

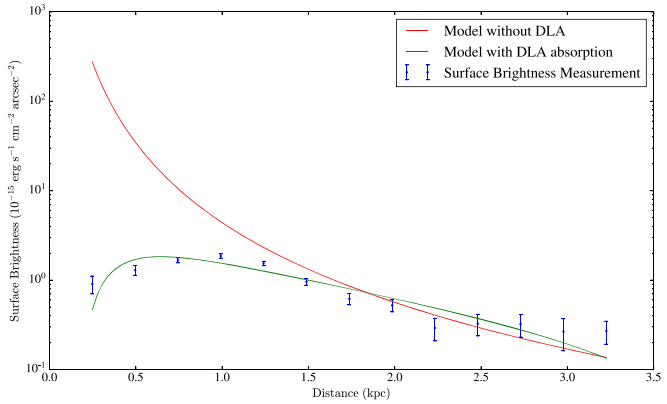

Figure 4. Surface brightness profile and models for the profile with and without DLA absorption around the quasar (centering at the quasar position). The red curve is the model for the SB profile centering at the position of quasar without DLA absorption, while the green curve is the model with DLA absorption. The model labeled in the green curve is the best-fitted model to the data of the SB measurement centering at the center of the quasar (labeled in blue).

systems, suggesting that the Lyα emission is not coming from the DLA galaxy.

4.2.3. *Fluorescent Lyα Emission*

The third possibility for the origin of the Lyα emission is fluorescent Lyα emission from the optically thick gas that is close to the DLA cloud or from a system detached from it. Ionizing photons intercepted by the gas ionize neutral hydrogen atoms and the subsequent recombination has a high probability ($\eta \sim 0.6$; e.g., Gould & Weinberg 1996) of ending up as Lyα photons.

We can estimate the SB I_α of the fluorescent Lyα emission through $\pi I_\alpha = h\nu_\alpha \eta f F_i / (1+z)^4$, where $h\nu_\alpha$ is the Lyα photon energy and the $(1+z)^4$ factor accounts for the cosmological dimming. For isotropic quasar emission, the ionizing photon flux F_i at the cloud position is $F_i = \int L_\nu / (h\nu) d\nu / (4\pi d^2)$, with L_ν being the quasar luminosity and d being the distance from the quasar to the gas cloud. The integral goes from the Lyman limit $\nu_L = 13.6\,\mathrm{eV}/h$ to infinity. The factor f is introduced to scale the line-of-sight (LOS) flux to that along the quasar-cloud direction, accounting for the anisotropy of the quasar emission of ionizing photons. With the assumption that $L_\nu = L_{\nu_L}(\nu/\nu_L)^{-\alpha}$, we have

$$I_\alpha = \frac{1}{(1+z)^4} \frac{1}{4\pi^2 d^2} \frac{\eta f}{\alpha} \frac{\nu_\alpha}{\nu_L} \nu_L L_{\nu_L}. \quad (1)$$

The quasar has $\nu_L L_{\nu_L} = 0.76 \times 10^{45}$ erg s^{-1} with $\alpha = 1.57$. For $d \sim 0.6$ kpc and $f \sim 0.1$, we obtain the Lyα SB to be at the level of 0.8×10^{-13} erg s^{-1} cm^{-2} arcsec^{-2}, which is about two orders of magnitude higher than the observed SB shown in Figure 2. To match the observation, we need to put the cloud much farther way from the quasar (e.g., $d > 10$ kpc along the LOS) or to have extremely anisotropic emission of the quasar (e.g., $f < 10^{-3}$).

The other difficulty faced by the fluorescent origin of the Lyα emission is the shape of the spectrum. Fluorescent Lyα photons emerging from the thin skin layer of the optically thick cloud would typically have a double-peak profile (e.g., Gould & Weinberg 1996; Zheng & Miralda-Escudé 2002; Adelberger et al. 2006), with peak separation about eight times the velocity dispersion in the cloud. If the velocity dispersion in the cloud is of the order of 50 km s^{-1} (e.g., Adelberger et al. 2006), the two peaks (with separation ~400 km s^{-1}) would be well resolved, which does not seem to be the case in the spectrum shown in Figure 1. The tentatively detected blue peak with low flux could indicate gas kinematics, like outflowing, in the cloud.

Overall, based on the Lyα SB and the Lyα line profile, we find that the fluorescent origin of the Lyα emission is not favored.

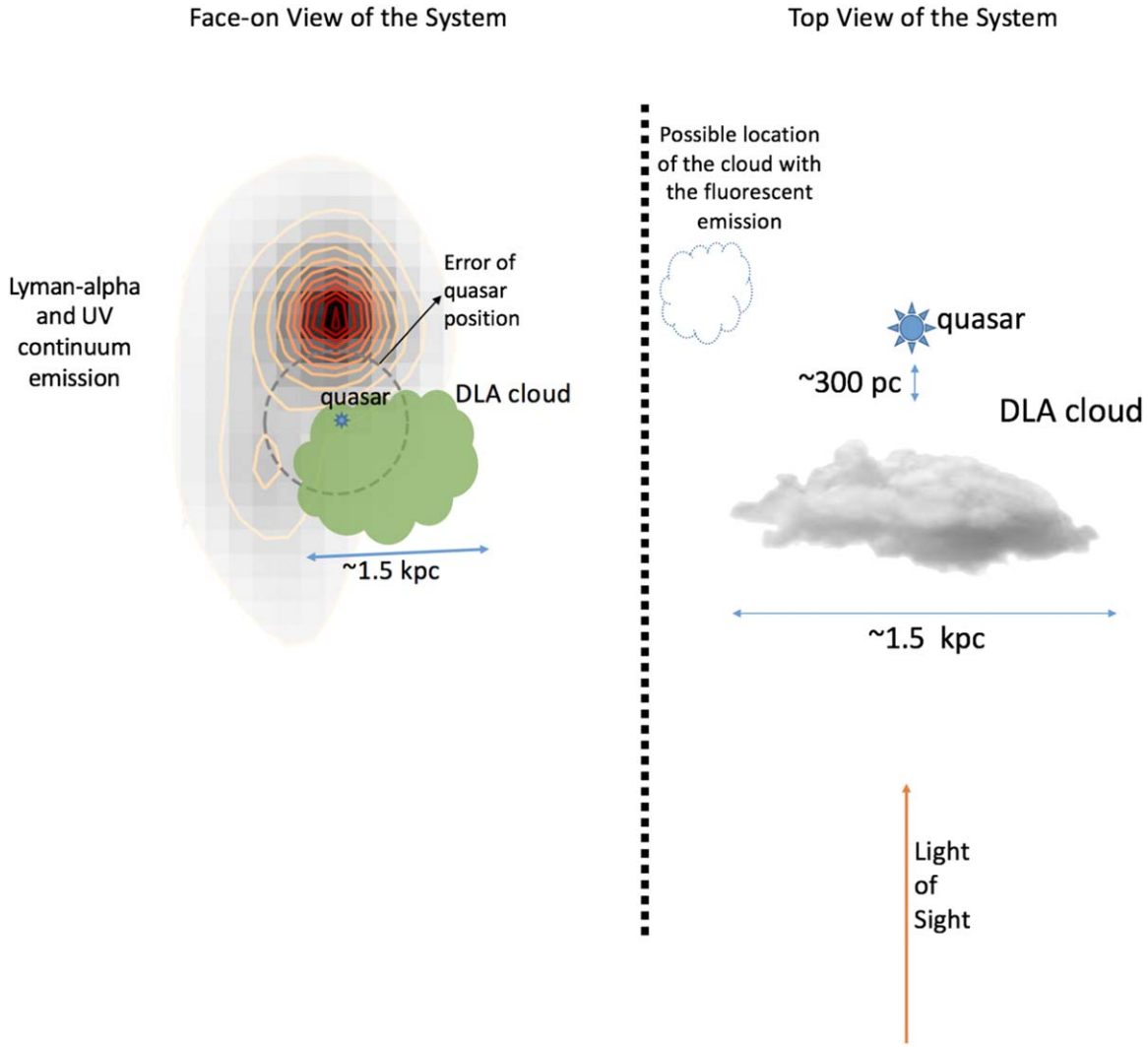

Figure 5. Cartoon illustration of the physical picture of the J1154–0215 system. Left panel: face-on view of the system. The contour plot is from the contour of the SB of the Sérsic fitting model. The DLA cloud is labeled in green with its size. The QSO position is labeled in blue, with its 1σ error labeled in gray. Right panel: top view of the system. The QSO is labeled in blue and the DLA cloud is labeled in white, with its size and distance from the QSO. The cloud in the dashed line shows the possible location of the gas cloud with the fluorescent emission for the less possible scenario that the fluorescent emission is the origin of the Lyα emission.

5. Conclusion and Future Observation

Combing six orbits of *HST* WFC3/UVIS FQ387N filter deep imaging with the spectrum (Figure 1), we conduct a pilot study on a target J1154–0215 with a PDLA system, i.e., J1154–0214. The narrow Lyα emission is revealed inside the DLA dark trough. We prefer the conclusion that this Lyα emission may come from the star-forming region of the QSO host galaxies. Future observations of the Hβ and other Balmer lines in the deep near-IR spectroscopy can help constrain the dust extinction. Furthermore, future IFU observations can help us to understand the gas kinematic structure of this system and thus further understand the interrelation between the central QSO, QSO host galaxies and the galactic environment of this target. In order to further confirm the origin of the Lyα emission, it is crucial to understand the polarization of the emission. Future facilities, including the Giant Magellan Telescope and Thirty Meter Telescope, will probe the polarization of these targets with reasonable exposure time and thoroughly distinguish the origin of the emission, shedding new light on the extended Lyα emission from star-forming regions or fluorescent emission from gases around QSOs.

We dedicate this article in memory of Hayley Finley, who left us a few days before this article was accepted. We wish to thank the anonymous referee for insightful comments that improved this Letter. We also acknowledge support from NASA through grant HST-GO-13818 from the Space Telescope Science Institute. We are grateful to acknowledge Luming Sun and Ning Jiang for sharing their insights on the future work of this Letter.

ORCID iDs

Jiani Ding https://orcid.org/0000-0003-4651-8510
Zheng Cai https://orcid.org/0000-0001-8467-6478
J. Xavier Prochaska https://orcid.org/0000-0002-7738-6875
H. Finley https://orcid.org/0000-0002-1216-8914
Xiaohui Fan https://orcid.org/0000-0003-3310-0131
Zheng Zheng https://orcid.org/0000-0003-1887-6732

References

Adelberger, K. L., Steidel, C. C., Kollmeier, J. A., & Reddy, N. A. 2006, ApJ, 637, 74
Bahcall, J. N. 1967, ApJL, 149, L7
Bennert, V. N., Treu, T., Auger, M. W., et al. 2015, ApJ, 809, 20
Bertin, E., & Arnouts, S. 1996, A&AS, 117, 393
Cai, Z., Fan, X., Jiang, L., et al. 2015, ApJL, 799, L19
Cai, Z., Fan, X., Noterdaeme, P., et al. 2011, ApJL, 736, L28
Cai, Z., Fan, X., Noterdaeme, P., et al. 2014, ApJ, 793, 139
Ciardullo, R., Gronwall, C., Wolf, C., et al. 2012, ApJ, 744, 110
Cooke, R., Pettini, M., Steidel, C. C., et al. 2010, MNRAS, 409, 679
Dijkstra, M., & Westra, E. 2010, MNRAS, 401, 2343
Fathivavsari, H., Petitjean, P., Jamialahmadi, N., et al. 2018, MNRAS, 477, 5625
Fathivavsari, H., Petitjean, P., Noterdaeme, P., et al. 2015, MNRAS, 454, 876
Fathivavsari, H., Petitjean, P., Noterdaeme, P., et al. 2016, MNRAS, 461, 1816
Finley, H., Petitjean, P., Pâris, I., et al. 2013, A&A, 558, A111
Gebhardt, K., Bender, R., Bower, G., et al. 2000, ApJL, 539, L13
Gould, A., & Weinberg, D. H. 1996, ApJ, 468, 462
Guaita, L., Gawiser, E., Padilla, N., et al. 2010, ApJ, 714, 255
Hennawi, J. F., Prochaska, J. X., Kollmeier, J., & Zheng, Z. 2009, ApJL, 693, L49
Hopkins, P. F., Somerville, R. S., Hernquist, L., et al. 2006, ApJ, 652, 864
Kennicutt, R. C., Jr. 1998, ARA&A, 36, 189
Koekemoer, A. M., Fruchter, A. S., Hook, R. N., et al. 2002, in The 2002 HST Calibration Workshop: Hubble after the Installation of the ACS and the NICMOS Cooling System, ed. S. Arribas, A. Koekemoer, & B. Whitmore (Baltimore, MD: STScI), 337
Lotz, J. M., Jonsson, P., Cox, T. J., & Primack, J. R. 2010, MNRAS, 404, 575
Matsuoka, Y., Strauss, M. A., Shen, Y., et al. 2015, ApJ, 811, 91
McConnell, N. J., & Ma, C.-P. 2013, ApJ, 764, 184
McLeod, K. K., & Bechtold, J. 2009, ApJ, 704, 415
Møller, P., Fynbo, J. P. U., Ledoux, C., & Nilsson, K. K. 2013, MNRAS, 430, 2680
Ouchi, M., Shimasaku, K., Akiyama, M., et al. 2008, ApJS, 176, 301
Prochaska, J. X., Chen, H.-W., & Bloom, J. S. 2006, ApJ, 648, 95
Reines, A. E., & Volonteri, M. 2015, ApJ, 813, 82
Schramm, M., Wisotzki, L., & Jahnke, K. 2008, A&A, 478, 311
Shapley, A. E., Steidel, C. C., Pettini, M., & Adelberger, K. L. 2003, ApJ, 588, 65
Silva, A. I., & Viegas, S. M. 2002, MNRAS, 329, 135
Targett, T. A., Dunlop, J. S., & McLure, R. J. 2012, MNRAS, 420, 3621
Yates, R. M., Kauffmann, G., & Guo, Q. 2012, MNRAS, 422, 215
Zheng, Z., & Miralda-Escudé, J. 2002, ApJ, 578, 33